9   DFT+DMFT for Oxide Heterostructures

Frank Lechermann

Institut für Theoretische Physik III

Ruhr-Universität Bochum

44780 Bochum

Contents

1   Introduction

The physics of transition-metal (TM) oxides is an ongoing highlight topic in condensed matter research, with its origins dating back to the earliest days of the quantum description of the solid state. The phenomenology spans from the various manifestations of basic electronic structure theory, i.e., conventional metallicity and band-insulating regimes, to the peculiar realizations of strong correlation mechanisms, as exemplified by, e.g., intriguing magnetic orderings and the discovery of unconventional superconducting phases. Beyond nature's original conception, the last 20-30 years witnessed an enormous boost in the fabrication of TM oxides, resulting in the nearly free design of nano-architectural combinations of individual oxide compounds (e.g. [1–4]).

This engineering path becomes especially interesting based on the fact that deviations from the conventional band-theory picture of weakly-interacting lattice electrons are most often encountered in bulk oxides with partially-filled TM(d) shells. Therefore by heterostructuring these materials, a unique playground for investigating, tailoring and eventually designing correlation effects may be opened. The challenges appear twofold in this context. First, *known* bulk-oxide correlation phenomena are transferred into the heterostructure environment and become tunable by various means. This, e.g., applies to magnetic, superconducting or further transport properties. Second, by interfacing different electronic bulk phases, *new* interface phases may emerge, possibly even without a distinct bulk analogon. A rather strict, obvious separation between these both research directions is albeit delicate.

In the first challenge, the proximity to an interface can enable, e.g., different structural/geometrical relaxations/constraints, symmetry breakings due to layering (cf. Fig. 1) or polarization effects because of a heterostructure-adapted electric field. Already a lot of work has been performed in this context and Refs. [5–7] may serve as overviews. For a concrete example, the physics of doped Mott insulators is a key research field in strongly correlated condensed matter. Bulk doping however poses many difficulties in view of a well-defined theoretical description. Most importantly, the intertwining with disorder mechanisms in the electronic and structural sector often hinders a straightforward modelling. Those problems may be overcome in Mott-oxide heterostructures, since electron-, hole-, or structural (i.e. effects only due to the different ion size of the valence-identical dopant) doping can nowadays be realized by respective doping layers. In this respect, the correlated doping physics becomes accessible in a well-defined manner by model-Hamiltonian and/or first-principles techniques. In general, accompanied by this progress, the examination of the influence of defects in strongly correlated materials has gained renewed interest, being explored by considering the detailed defect chemistry together with a state-of-the-art treatment of electronic correlations.

The second challenge is even more demanding and highlight examples in this regard might be provided by the physics of conducting quasi-two-dimensional electron interface systems (2DES) emerging in oxide heterostructures consisting of bulk band insulators. But the clarification of the uniqueness of such engineered electron phases beyond respective bulk counterparts is still a matter of frontline research. Furthermore, topological nontrivial electronic states are
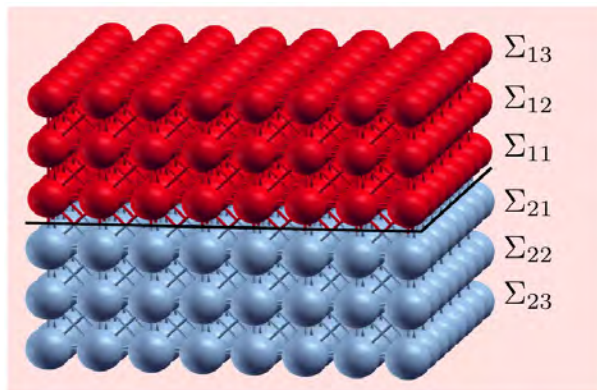
Fig. 1: *Principle issue of symmetry breaking induced by an interface between to oxide materials joint in an heterostructure architecture, leading to layer-dependent electronic self-energies Σ_{ij}.*

surely also to be considered in the oxide-heterostructure context, but the explicit interplay between topology and electronic correlations is still largely uncharted territory. In the following, these latter material possibilities will not be covered, but the interested reader finds ideas on this in a recent review [8].

The present brief overview on the first-principles many-body description of oxide heterostructures focusses on the applicative physics aspect, and is not intended to provide a thorough introduction to the DFT+DMFT formalism. The interested reader in view of this main theoretical/methodological aspect is referred to other chapters within the extended series of the Jülich School. We here provide only a very short summary on the key features of the DFT+DMFT framework in section 2. The sections 3, 4 and 5 deal with different applications and the specific physics of selected oxide heterostructure problems. Since the existing general theoretical work in this field is rather extensive, the given short review cannot provide a comprehensive and detailed survey. Instead, focus is here mainly on the corresponding work, directly associated with the author.

2 DFT+DMFT in a nutshell

The electronic density functional theory marks one cornerstone in condensed matter research, and will remain a key step in the atomistic investigation of matter. In essence, the problem of interacting electrons is mapped within DFT onto the problem of noninteracting particles within a complicated effective potential. In the present context it is vital to note that although DFT represents *in principle* a complete many-body account of interacting electrons, the most common Kohn-Sham representation based on the local-density or generalized-gradient approximations (i.e. LDA or GGA) brand this method as an effective single-particle approach. For condensed matter problems, it therefore describes electrons via band-theory arguments, and the original many-body effects due to the mutual Coulomb repulsion between electrons are cast into the aforementioned effective single-particle potential.
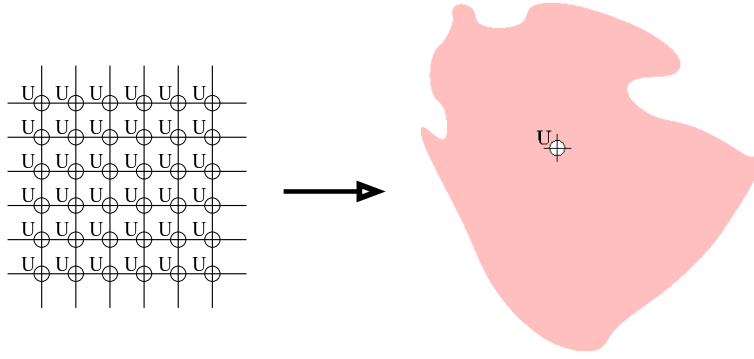
Fig. 2: *Sketch of the DMFT mapping of an interacting lattice problem (left) onto a problem of an impurity within an energy-dependent bath (right), assuming a sole onsite Coulomb interaction U, and hopping t between neighboring sites.*

Dynamical mean-field theory [9, 10] can be seen as the quantum many-body scheme for correlated electrons with the best compromise between generality, accuracy and performance. Notably, also DMFT describes a mapping, i.e., from the problem of interacting lattice electrons onto the problem of a quantum impurity embedded within a self-consistent energy-dependent bath, as sketched for the Hubbard model in Fig. 2.

For chemical potential μ, and Hamiltonian $H(\mathbf{k})$ at wave vector $\mathbf{k}$, the one-particle Green function reads

$$G(\mathbf{k}, i\omega_{\mathrm{n}}) = \left(i\omega_{\mathrm{n}} + \mu - H(\mathbf{k}) - \Sigma(\mathbf{k}, i\omega_{\mathrm{n}})\right)^{-1}, \tag{1}$$

where $\omega_{\mathrm{n}} := (2n+1)\pi T$ are fermionic Matsubara frequencies employed to emphasize the treatment at *finite* temperature. The analytical continuation to real frequencies ω in actual calculations may, e.g., be performed via the maximum entropy method (see e.g. [11, 12] for more details).

The local Green function is approximated in DMFT with the help of a k-independent impurity self-energy $\Sigma_{\mathrm{imp}}(i\omega_{\mathrm{n}})$, i.e.,

$$G_{\mathrm{loc}}^{\mathrm{DMFT}}(i\omega_{\mathrm{n}}) = \sum_{\mathbf{k}} \left(i\omega_{\mathrm{n}} + \mu - H(\mathbf{k}) - \Sigma_{\mathrm{imp}}(i\omega_{\mathrm{n}})\right)^{-1}, \tag{2}$$

and the corresponding impurity problem reads

$$\Sigma_{\mathrm{imp}}(i\omega_{\mathrm{n}}) = \mathcal{G}_0(i\omega_{\mathrm{n}})^{-1} - G_{\mathrm{imp}}(i\omega_{\mathrm{n}})^{-1}. \tag{3}$$

The so-called Weiss field $\mathcal{G}_0(i\omega_{\mathrm{n}})$ is a unique function of the local Hamiltonian (expressed within a localized basis) and the DMFT self-consistency condition implies $G_{\mathrm{imp}} = G_{\mathrm{loc}}^{\mathrm{DMFT}}$. The calculational loop is depicted in the 'DMFT loop' box of Fig. 3. Quantum-impurity solvers based, e.g., on quantum Monte Carlo, Exact Diagonalization, etc. yield the solution. For more details we refer to [12] for an early review. Note that local-interaction diagrams are included to all orders in this non-perturbative theory. The vital energy dependence of the Weiss field ensures the qualitatively correct description of low-energy quasiparticle (QP) features as well as high-energy incoherent (Hubbard) excitations.
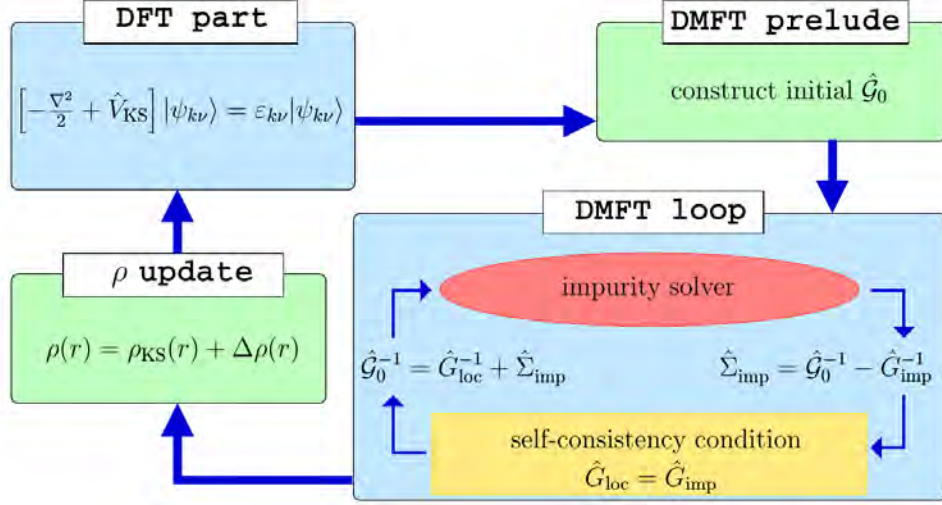
Fig. 3: *State-of-the-art charge self-consistent DFT+DMFT loop (after [21]). The calculation usually starts from a self-consistent Kohn-Sham solution. The correlated subspace is defined and the initial Weiss field $\mathcal{G}_0$ constructed. Afterwards, a single (or more) DMFT step is performed. The obtained self-energies are upfolded and an updated charge density $n(\mathbf{r})$ is computed. A new charge density implies a new Kohn-Sham potential, and a single new Kohn-Sham step is performed, therefrom a new Weiss field is generated, etc..*

In the hybrid scheme of DFT+DMFT [13, 14], the many-body part incorporates a Hubbard-model(-like) picturing of a suitably chosen *correlated subspace* [15, 16]. This correlated sub-space is understood as a quantum-numbered real-space region where correlated electrons tend to reside. The key interfacing blocks of the complete DFT+DMFT self-consistency cycle [17–20] (cf. Fig. 3) are marked by the downfolding of the full-problem Bloch space to the correlated subspace, and the upfolding of the DMFT self-energy back to the original space. The main corresponding formulas for sites $\mathbf{R}$, local orbitals mm' and band indices $\nu\nu'$, read

$$G_{mm'}^{\mathbf{R},\mathrm{imp}}(i\omega_{\mathrm{n}}) = \sum_{\mathbf{k},(\nu\nu')\in\mathcal{W}} \bar{P}_{m\nu}^{\mathbf{R}}(\mathbf{k})\, G_{\nu\nu'}^{\mathrm{bloch}}(\mathbf{k}, i\omega_{\mathrm{n}})\, \bar{P}_{\nu'm'}^{\mathbf{R}*}(\mathbf{k})\,, \tag{4}$$

$$\Delta\Sigma_{\nu\nu'}^{\mathrm{bloch}}(\mathbf{k}, i\omega_{\mathrm{n}}) = \sum_{\mathbf{R},mm'} \bar{P}_{\nu m}^{\mathbf{R}*}(\mathbf{k})\, \Delta\Sigma_{mm'}^{\mathbf{R},\mathrm{imp}}(i\omega_{\mathrm{n}})\, \bar{P}_{m'\nu'}^{\mathbf{R}}(\mathbf{k})\,, \tag{5}$$

with $\bar{P}$ denoting the normalized projection between Bloch space and correlated subspace [15]. The object $\Delta\Sigma_{\nu\nu'}^{\mathrm{bloch}}$ describes the k-dependent self-energy in Bloch space after double-counting correction (which takes care of the fact that some correlations are already handled on the DFT level). Note that there is a choice for the range $\mathcal{W}$ of included Kohn-Sham bands in the down-folding. In the upfolding operation, the charge density will also be affected by correlation effects, i.e.,

$$\rho(\mathbf{r}) = \sum_{\mathbf{k},\nu\nu'} \langle\mathbf{r}|\Psi_{\mathbf{k}\nu}\rangle \Big(f(\tilde{\epsilon}_{\mathbf{k}\nu})\,\delta_{\nu\nu'} + \Delta N_{\nu\nu'}(\mathbf{k}) \Big) \langle\Psi_{\mathbf{k}\nu'}|\mathbf{r}\rangle\,, \tag{6}$$

where Ψ denotes Kohn-Sham states, f the associated Fermi function and ΔN is the DMFT self-energy correction term [21, 15]. Note finally that this first-principles many-body scheme works, at heart, at finite temperature T. Electron states are therefore subject to the full thermal impact, beyond sole occupational Fermi-function modification.

In oxide heterostructures, as in various other multi-atom unit-cell problems, the correlated sub-space invokes not only a single lattice site. In the case of symmetry-equivalent sites, the self-energy is determined for a representative site and transferred to the remaining sites via proper symmetry relations. A different impurity problem is defined for each symmetry-inequivalent site j through [22]

$$\mathcal{G}_0^{(j)}(i\omega_n)^{-1} = G^{(j)}(i\omega_n)^{-1} + \Sigma_{imp}^{(j)}(i\omega_n) \quad , \tag{7}$$

and the coupling is realized via the DFT+DMFT self-consistency condition invoking the computation of the complete lattice Green function.

If not otherwise stated, the materials investigations discussed in sections 3, 4 and 5 involving the author were performed using charge-selfconsistent DFT+DMFT based on a mixed-basis pseudopotential code [23] and hybridization-expansion continuous-time quantum Monte Carlo [24] in the TRIQS package [25] as an impurity solver. For more technical details on the implementation the reader is referred to Ref. [20].

3   Band-insulator/band-insulator heterostructure

An emerging metallic two-dimensional electron system (2DES) at the n-type interface between band-insulating LaAlO$_3$ (LAO) and SrTiO$_3$ (STO) discovered by Ohtomo and Hwang [2] marks one of the most appreciated discoveries in the oxide-heterostructure context. A polar-catastrophe mechanism [26] is believed to be dominantly at the root of the 2DES establishment. In terms of electronic correlations, this and related interface systems between band insulators [27] appear quite subtle since the basic constituents do not already host strongly correlated electrons in partially-filled d- or f-states. However, the follow-up experimental studies revealed, e.g., the possibility for superconductivity [28] as well as magnetic order [29] in the LAO/STO interface, which may be fingerprints for the relevance of electronic correlations. Furthermore, defect-related physics is believed to be important in these interfaces, which can directly induce local-based self-energy effects beyond the effective single-particle realm.

3.1   LaAlO$_3$/SrTiO$_3$: defect-free interface

Interface metallicity is easily achieved within DFT for the stoichiometric defect-free (DF) LAO/STO (see Fig. 4b,c). Two electrons occupy the dominant Ti($3d$) low-energy manifold, matching the number for the polar-catastrophe avoidance, which predicts Ti$^{3.5+}$O$_2^{4-}$ at the interface [26]. Figure 4b shows that the electrons which form the 2DES are confined to the STO part, with dominant localization near Ti$^{(12)}$, i.e., directly at the boundary towards the LAO part. There, the major orbital Ti($3d$) character is of d_{xy} kind.

Note that although there is an apparent effect of larger onsite Hubbard interactions on the quasiparticle formation/shape as visualized in Fig. 4d, sizable spectral-weight transfer to higher energies far from the Fermi level remains absent in the DF case. This is understandable from the highly fractional filling of the interface Ti-d_{xy} orbitals. Note also that in either case, DFT or DFT+DMFT level, the DF system remains far from a ferromagnetic (FM) instability.
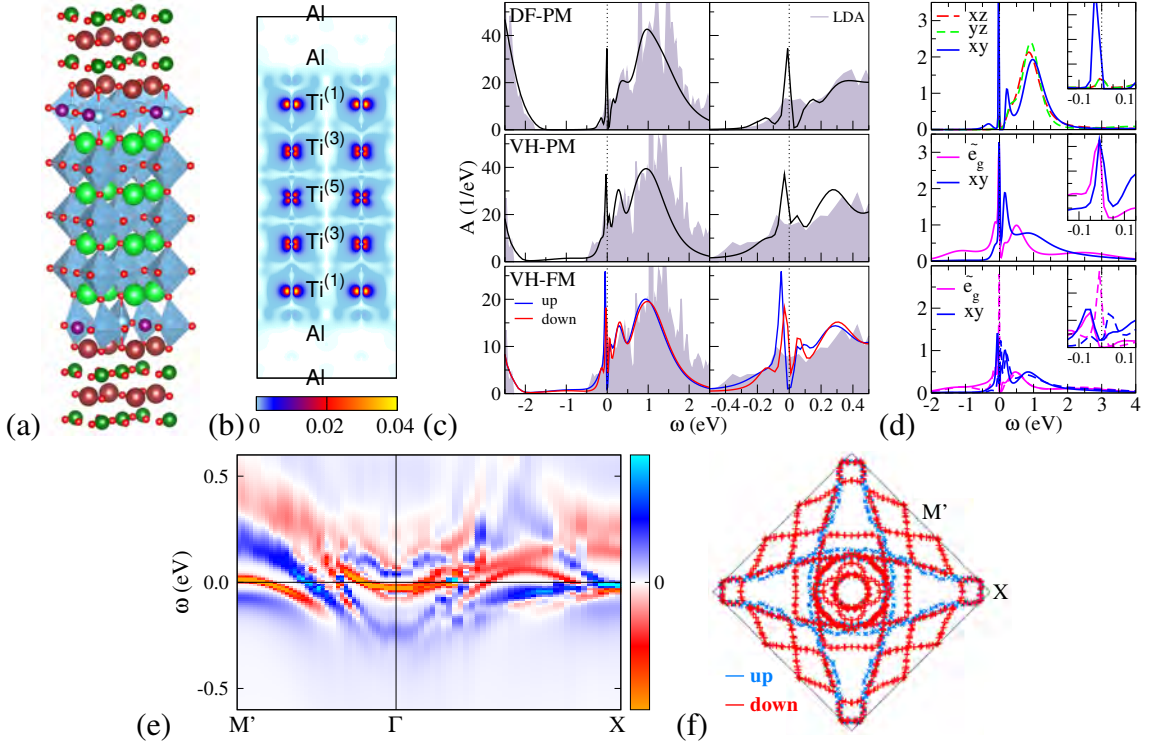
Fig. 4: *Influence of oxygen vacancies in the LAO/STO interface based on DFT+DMFT calculations for a dense-defect scenario (after [30]). (a) 80-atom superlattice, La (brown), Al (dark green), Sr (green), Ti (blue), O (red), OV (violet). (b) DFT valence charge density of the occupied low-energy manifold in the DF structure. (c) Total spectral function, left: larger window, right: smaller window. Top: defect-free paramagnetic (DF-PM), middle: vacancy-hosting paramagnetic (VH-PM) and bottom: vacancy-hosting ferromagnetic (VH-PM). (d) Local spectral function for selected effective Ti(3d) states, vertical ordering as in (c). (e) spin contrast of the k-dependent spectral function $A(\mathbf{k}, \omega)$ in the ferromagnetic phase. (f) FM Fermi surface.*

3.2 LaAlO$_3$/SrTiO$_3$: oxygen-deficient interface

While the clean interface hosts the polar-catastrophe scenario but lacks strong (local) electron correlation effects, things change when allowing for defects at or near the interface. For instance, relevant local correlations are evident from the co-appearance of oxygen vacancies and ferromagnetism in LAO/STO [31]. Point defects are in fact an important ingredient of the interface physics between band-insulating systems. In this regard, oxygen vacancies (OVs) so far appear to have the major impact [32]. In a DFT+DMFT study of the LAO/STO interface [30] it is shown that stable ferromagnetic order builds up on both, OVs *and* electronic correlations. While Ti-$3d(t_{2g})$ orbitals dominate the states directly above the STO gap, an oxygen vacancy leads to an in-gap state of Ti-$3d(e_g)$ kind, here termed $\tilde{e}_g$. In a minimal model, the correlated electronic structure at the interface may be described by the interplay between $\tilde{e}_g$ and an in-plane xy orbital from the t_{2g} threefold (see Fig. 4). A reduced Hubbard $U = 2.5\,\mathrm{eV}$ and Hund's exchange $J_\mathrm{H} = 0.5\,\mathrm{eV}$ is appropriate to elucidate this physics in the smaller correlated subspace. Note that a dense-defect scenario is assumed in that superlattice assessment, i.e., there is an OV at every other O site in the interface TiO$_2$ plane. Still, an in-gap $\tilde{e}_g$-like state at $\varepsilon_\mathrm{IG} \sim -1.2\,\mathrm{eV}$ is well reproduced in agreement with experiment [33]. This finding was also verified by even
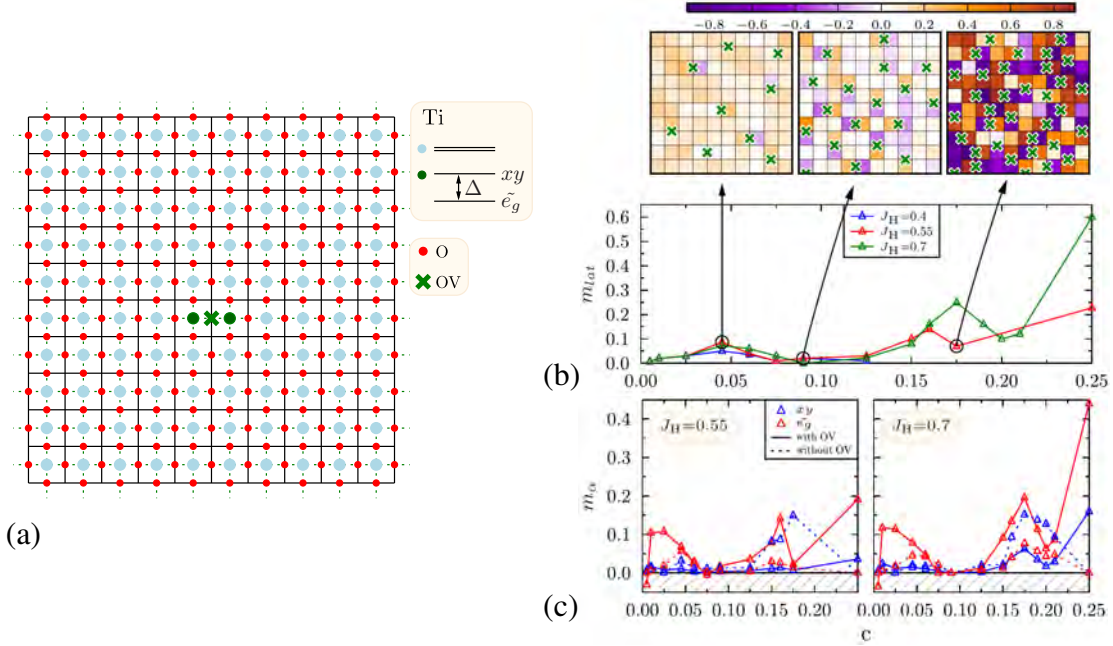
Fig. 5: *Influence of oxygen vacancies in the LAO/STO interface (after [35]). (a) Model setting:* 10×10 *square lattice, two orbitals per site, oxygen degrees of freedom are integrated out, nearest-neighbor hopping* $t = 0.2\,eV$*. A crystal-field splitting* $\Delta = 0.3\,eV$ *between* $\tilde{e}_g$ *and* xy *is applied, if an OV is located nearby. (b) Top: color-coded ordered local magnetic moments on the lattice for selected OV concentration. Bottom: lattice net moment per site for different Hund's exchange* J_H*. (c) Orbital-resolved magnetic moment, averaged per site.*

larger supercell calculations [34]. Close to an oxygen vacancy, the formal oxdiation state of titanium is close to Ti^{3+}, i.e., locally a $3d^1$ occupation is realized by the appearance of defects. But the emergent spin polarization in the given dense-defect limit in not of purely local kind, it develops substantial dispersive behavior in reciprocal space (cf. Fig. 4d,e). In general, these defect-based studies show that strong electron correlations, describable within DFT+DMFT, may be introduced also in band-band insulator architectures of oxide heterostructures.

Approaching significantly lower OV concentrations in a first-principles manner asks for the handling of much larger supercells. Due to the numerical heaviness of DFT+DMFT, this is yet not easily achievable. Therefore instead, a model-Hamiltonian approach equipped with the relevant ingredients from the dense-defect limit, appears more adequate. Figure 5 displays the setting and some main results of such an ansatz [35]. A two-orbital $\tilde{e}_g$-xy Hubbard model is solved on a 10×10 square lattice resembling the TiO_2 interface plane. The efficient rotational-invariant slave boson (RISB) scheme [36, 37], employing a self-energy which has a linear-in-frequency term and a static contribution, is put into practice for a simplified treatment of the correlation problem. Focussing on the magnetic order, it can be shown that there are three regimes with growing number of OVs. At very small concentration, a Ruderman-Kittel-Kasuya-Yoshida (RKKY) coupling leads to FM order, whereas at larger concentration a double-exchange mechanism dominates a different FM phase. In-between local antiferromagnetic (AFM) pairs (or, in an advanced self-energy modeling, possibly cluster singlets) result in a nearly absent net magnetic moment. This intricate and highly nontrivial OV-dependent magnetic exchange is in line with experimental findings of a strongly probe-dependent magnetic response.
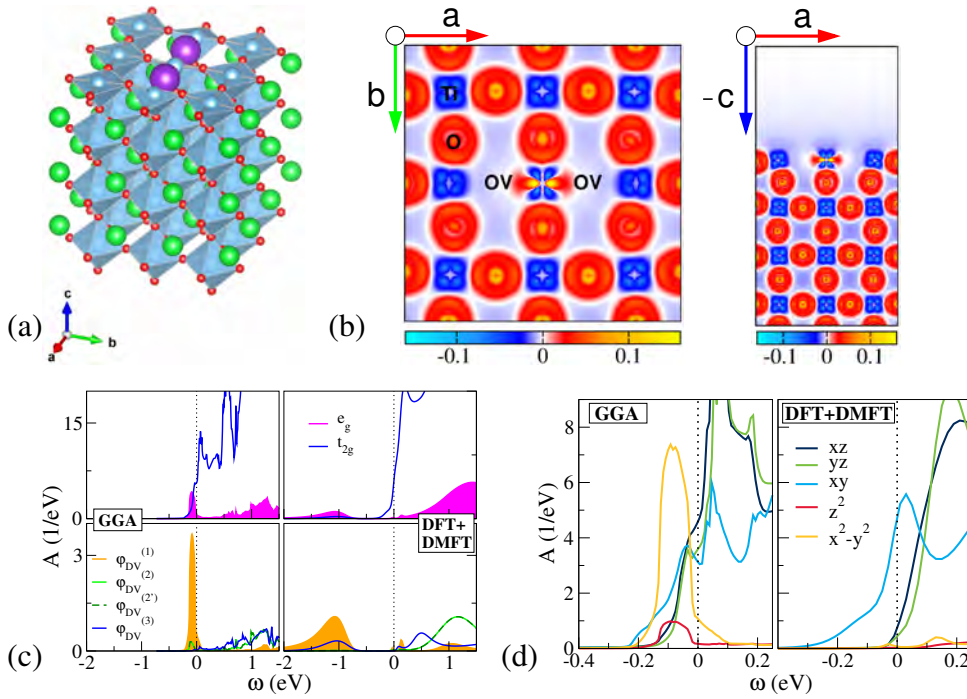
Fig. 6: *Influence of a double vacancy in the SrTiO₃ (001) surface (after [38]). (a) 180-atom supercell with a TiO₂-terminated surface layer of STO: Sr (green), Ti (blue), O (red), OV (violet). (b) Bond charge density $n_{\text{total}}(\mathbf{r}) - n_{\text{atomic}}(\mathbf{r})$: top view (left), side view (right). (c) Spectral-weight comparison of the summed Ti(t_{2g},e_g) (top) and of the dominant Ti-based effective orbital between DFT(GGA) (left) and DFT+DMFT (right). The $\varphi_{\text{DV}}^{(1)}$ Wannier-like orbital is an effective inplane e_g orbital located on the Ti site between the OVs. (d) Low-energy spectral-weight comparison of the Ti($3d$) states.*

3.3 Oxygen-deficient SrTiO₃ surface

In parallel to the STO-based heterostructure investigations, studying the SrTiO₃ surface attracted significant attention. Interface and surface properties of a chosen oxide are often related and the comparison between both planar-extended defects to the bulk enables a better understanding of emergent phenomena. A 2DES was initially also found on the oxygen-deficient (001) surface [39, 40] and soon after also confirmed for other cleavage planes, e.g., in (111) direction [41]. As a difference to the LAO/STO interface, the defect-free STO surface is believed to be insulating. Due to a missing interface-driven polar-catastrophe mechanism, again defects such as OVs are essential to metallize the surface. Similar to the interface spectrum, an in-gap state at a very similar position, i.e. ~ -1.3 eV, has been detected on the STO surface early on [42]. Recent DFT+DMFT considerations of the STO(001) surface with OVs indeed verified this in-gap state [38], which is again dominantly formed by Ti-$3d$(e_g) weight. (cf. Fig 6). Furthermore, the low-energy structure dominated by Ti-$3d$(t_{2g}) states is also in accordance with experiment. A double-vacancy defect provided the best matching with experiment, however only two distinct vacancy configuration were examined because of the large numerical effort within DFT+DMFT. Nonetheless, the spectral separation of e_g at high energy and t_{2g} is a clear generic feature of the study. Note that conventional DFT is not sufficient to provide this orbital separation (cf. Fig. 6c,d).
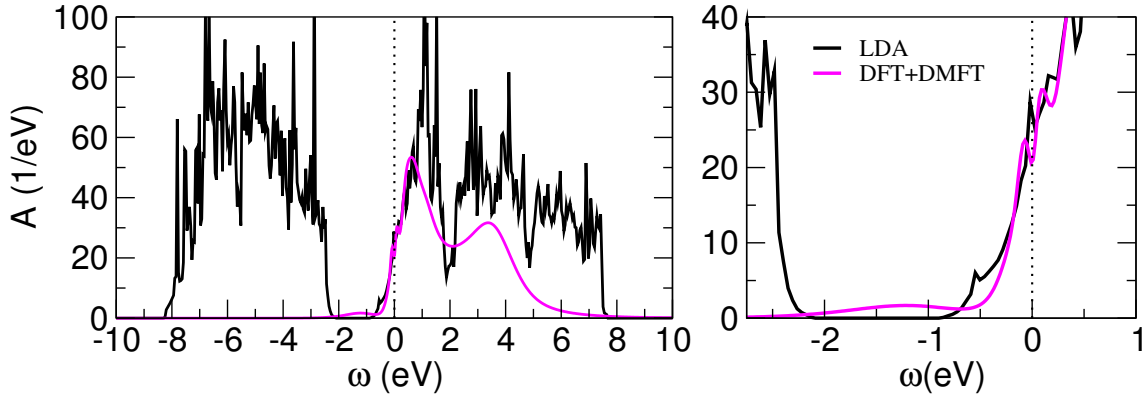
Fig. 7: *Spectral information for a LaTiO$_3$/SrTiO$_3$ superlattice with 4 SrO and 4 LaO layers (after [43]). Left: total spectrum, right: closer to Fermi level.*

4 Mott-insulator/band-insulator heterostructure

4.1 LaTiO$_3$/SrTiO$_3$

Oxide heterostructures composed of a Mott insulator and a band insulator have also been studied early on, initially via experimental work on the LaTiO$_3$/SrTiO$_3$ (LTO/STO) interface [44]. Contrary to the previous combination of pure band insulators, the Mott-insulating part of course injects the correlated electron problem into the heterostructure architecture right from the start. While STO is an ideal cubic perovskite at ambient temperature, LTO marks a distorted perovskite with orthorhombic crystal symmetry. Initial model-Hamiltonian Hartree-Fock studies of a Hubbard-model application to such an interface yielded an intricate phase diagram with the number of La-layers and Hubbard U [45]. Simplified realistic DMFT for LTO/STO [46] emphasized the structural orthorhombic-versus-tetragonal aspect of the LTO part. Transport within a Mott-band insulator heterostructure has also been studied again within a model-Hamiltonian approach [47].

A superlattice DFT+DMFT investigation of LTO/STO [43] revealed the realistic competition of both insulating systems stacked along the c-axis, giving rise to a metallic interface state. The correlated subspace can be chosen to be spanned by Ti-$3d(t_{2g})$ states, i.e., consists locally of three correlated orbitals. A Hubbard $U = 5$ eV and Hund's exchange $J_{\rm H} = 0.7$ eV is applied in that subspace. Orbital-dependent charge transfers lead to a strong Ti-$3d(xy)$, i.e., inplane electronic polarization in the interface TiO$_2$ layer. Surely, on the STO side the Ti^{4+} oxidation state with nominal $3d^0$ occupation is quickly reached, while on the LTO side the Ti^{3+}-$3d^1$ establishes and a sizably lower Hubbard band at ~ -1.1 eV is identified in the spectral function (see also Fig. 7). In those calculations, the lattice constant was fixed to the cubic STO value, but local structural relaxations on the DFT level were allowed. It is to be noted that the lattice degrees of freedom are an important aspect in oxide heterostructures. Simplified DFT+DMFT bulk-like studies revealed, e.g., the impact of strain on the Mott-insulating state of LaTiO$_3$ [48] and LaVO$_3$ [49].
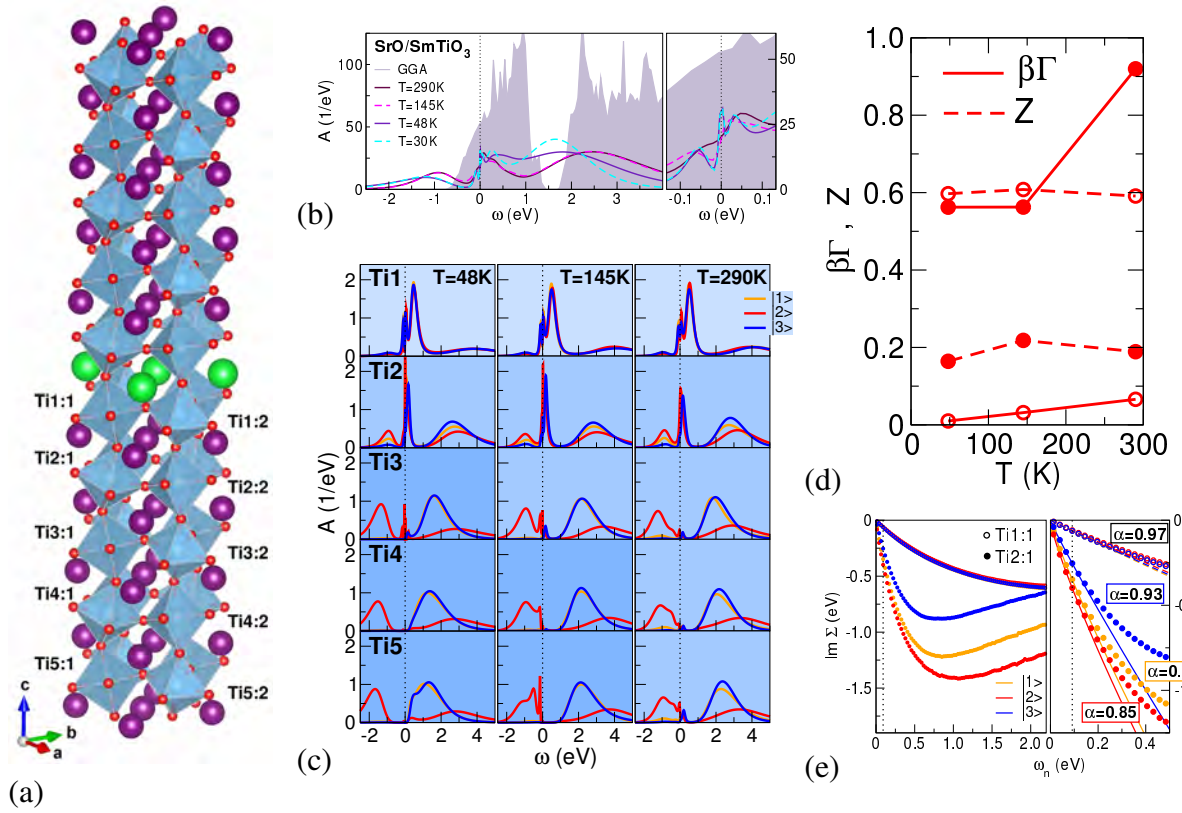
Fig. 8: *Paramagnetic DFT+DMFT data of δ-doping SmTiO$_3$ with a SrO monolayer (after [50]). (a) 100-atom unit cell in a superlattice architecture: Sr (green), Sm (purple), Ti (blue), O (red). Two inequivalent Ti sites are handled in each TiO$_2$ layer. Structural relaxations are performed on the DFT(GGA) level. (b) Total spectral function at different temperatures. (c) Layer-, orbital- and T-resolved spectral function. The correlated subspace consists of three effective t_{2g} orbitals at each Ti site. (d) QP weight Z and dimensionless electron-electron scattering rate $\beta\Gamma = -Z\,\mathrm{Im}\,\Sigma(i0^+)$ for the dominant state $|2\rangle$ in the first (open circles) and second (filled circles) TiO$_2$ layer. (e) Orbital-resolved imaginary part of the self-energy on the Matsubara axis. Left: larger frequency range, right: low-frequency region with fitting functions $\mathrm{Im}\,\Sigma(\omega_{\mathrm{n}}) = C_0 + A\,\omega_{\mathrm{n}}^\alpha$ (dashed/full lines). Exponential-fitting cutoff n_c is denoted by the dotted line. Values $\alpha = 1$ and $C_0 = 0$ mark the Fermi-liquid regime.*

4.2 δ-doping of titanate Mott insulators

Even more intriguing physics may be found when starting directly from a doped-Mott state within the heterostructure setting. Motivated by experimental work [51–53], a first-principles many-body investigation of δ-doping the rare-earth titanates LaTiO$_3$, GdTiO$_3$ and SmTiO$_3$ with a single SrO layer was undertaken [54, 50]. Especially the δ-doped SmTiO$_3$ case displays puzzling physics in experiment, namely NFL transport that switches to FL-like characteristics upon adding further SrO layers. In the rare-earth titanate $3d(t_{2g}^1)$ series of distorted-perovskite Mott insulators, the magnetic low-temperature state changes from AFM to FM with the size of the rare-earth ion. The samarium titanate is still AFM, but just on the border towards ferromagnetism. Structurally well-defined hole doping introduced by the SrO monolayer renders SmTiO$_3$ metallic. The DFT+DMFT results (see Fig. 8) reveal significant spectral-weight trans-
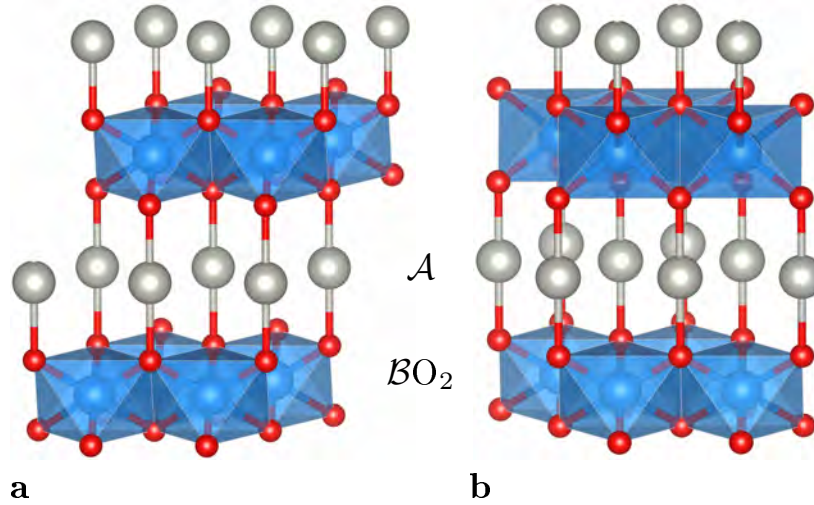
Fig. 9: *Delafossite $\mathcal{A}\mathcal{B}O_2$ crystal structure. (a) $R\bar{3}m$ and (b) $P6_3/mmc$ symmetry. $\mathcal{A}$ (grey), $\mathcal{B}$ (blue) and O (red). From Ref. [57].*

fer to higher energies compared to DFT, and in addition a complex layer-resolved electronic structure. While far from the doping layer the system resides in an orbital-polarized Mott-insulating state, it is conducting in an orbital-balanced manner just at the interface TiO_2 layer (cf. Fig. 8c). Both regimes are joined by an orbital-polarized doped-Mott layer with a largely renormalized QP peak at the Fermi level. A detailed analysis of the layer- and orbital-dependent self-energies shown in Fig. 8d,e indeed reveals signatures of a non-Fermi-liquid (NFL) exponent for the dominant effective t_{2g} orbital in the second, i.e., orbital-polarized doped-Mott, TiO_2 layer. Further investigations hint towards competing AFM-FM fluctuations in the Mott-critical zone as a possible cause for NFL behavior [50]. A pseudogap(-like) structure in the theoretical spectral function subject to such fluctuations has indeed been identified in experimental studies [55]. In an extension of this study, it was shown that the addition of further SrO layers establishes an extra band-insulating regime in the formed $SrTiO_3$-like region, with a stronger inplane xy-polarized metallic layer at the boundary [56].

5   Natural oxide heterostructures: delafossites

Delafossites, named after the french crystallographer Gabriel Delafosse (1796-1878), are oxides of type $\mathcal{A}\mathcal{B}O_2$, where $\mathcal{A}$ and $\mathcal{B}$ denote different metallic elements. Their unique crystal structure (see Fig. 9) consists of an alternate stacking of triangular $\mathcal{A}$ lattices and planes of edge-sharing $\mathcal{B}O_6$ octahedra along the c-axis. Importantly these two different layer types are connected via oxygen in a so-called dumbbell position. There are two possible stacking types, namely the more common rhombohedral one with $R\bar{3}m$ space-group symmetry and the hexagonal one giving rise to $P6_3/mmc$ symmetry. The metallic ions are in the formal oxidation state $\mathcal{A}^+$ and $\mathcal{B}^{3+}$, respectively.

Delafossites split into a larger insulating and a smaller metallic class of compounds. In a series of papers [58–60], Shannon *et al.* in 1971 described the novel synthesis and single-crystal growth of several delafossites with $\mathcal{A}$=Pd, Pt and Ag. Among those, there are oxides with

exceptionally high electrical conductivity at room temperature, e.g., $PdCoO_2$ and $PtCoO_2$, in combination with an outstanding single-crystal purity. This combined feature of such delafossites has started to become an intense field of research in recent years (see e.g. Refs. [61, 62] for reviews). That specific group of delafossites in terms of metallic properties, includes also the $PdCrO_2$ compound, which, among further challenging physics, hosts Mott-insulating CrO_2 layers [63–65].

This brings us to a very relevant aspect in view of our general heterostructure context. The delafossite architecture gives rise to a natural heterostructure, in which individual layers may attain a distinct character of their own. In most known layered materials, e.g., cuprates, cobaltates, etc., there is usually one 'active' layer and the remaining part mainly provides the glue. However in delafossites, e.g., the $\mathcal{A}$ layer can manage the metallic transport, while the $\mathcal{B}O_2$ layers account for the magnetic ordering. This not only entails exciting physical processes in the pure compound, but furthermore possibly allows for a kind of 'meta oxide-heterostructure' physics upon additional (nano-)engineering.

5.1   Basic DFT characterization

Let us first focus on a DFT assessment of selected Co- and Cr-based delafossites. Figure 10 displays the band theoretical results for the spectrum of $PdCoO_2$, $PdCrO_2$ and $AgCrO_2$, namely density of states (DOS) and band structures. For $PdCoO_2$ we also provide plots of the Wannier-like $Pd(4d)$ orbitals. In that compound, the $Pd(4d)$ states are largely occupied with a bandwidth (W) hierarchy of $W_{a_{1g}} > W_{e'_g} > W_{e_g}$. As shown in Fig. 10b, the $Co(3d)$ weight is mostly located in the bands close to and above the Fermi level ε_F, with a single band crossing ε_F. The latter dispersion, denoted in the following 'cPd', is dominantly of mixed $Pd(4d)$ and partial $Co(3d)$ kind. Note that the e'_g orbitals are the ones with the strongest in-plane character (see Fig. 10b). Though the band-filling $Co(3d)$ character resembles an original $Co(3d^6)$ picture, from the hybridizations at the Fermi level a completely inert Co-t_{2g} subshell is not truly justified. The DFT fermiology and dispersions at low energy are in good agreement with data from angle-resolved photoemission spectroscopy (ARPES) measurements [66] and de Haas-van Alphen studies [67]. Thus plain DFT seemingly provides already an adequate description of key $PdCoO_2$ features.

Contrary to $PdCoO_2$, the $\mathcal{B}$-site states of $Cr(3d)$ character are much less filled, the three t_{2g}-dominated bands are right at the Fermi level, and the $Pd(4d)$ character at ε_F is minor (see Figs. 10c, d). This however strongly disagrees with available experimental data from ARPES [68, 63] and quantum oscillations [69, 70]. In experiment, there is also only a single band crossing the Fermi level, quite similarly as in $PdCoO_2$. This discrepancy is due to the neglect of strong electronic correlations in conventional DFT, which misses the Mott-localized character of the CrO_2 layers. Partial agreement with experiment concerning the dispersions can be achieved within spin-polarized DFT [71, 68, 63, 72], accounting also for the magnetic ordering at low temperatures. But this Slater-type handling of the $Cr(3d)$ states is not describing the underlying physics comprehensively.
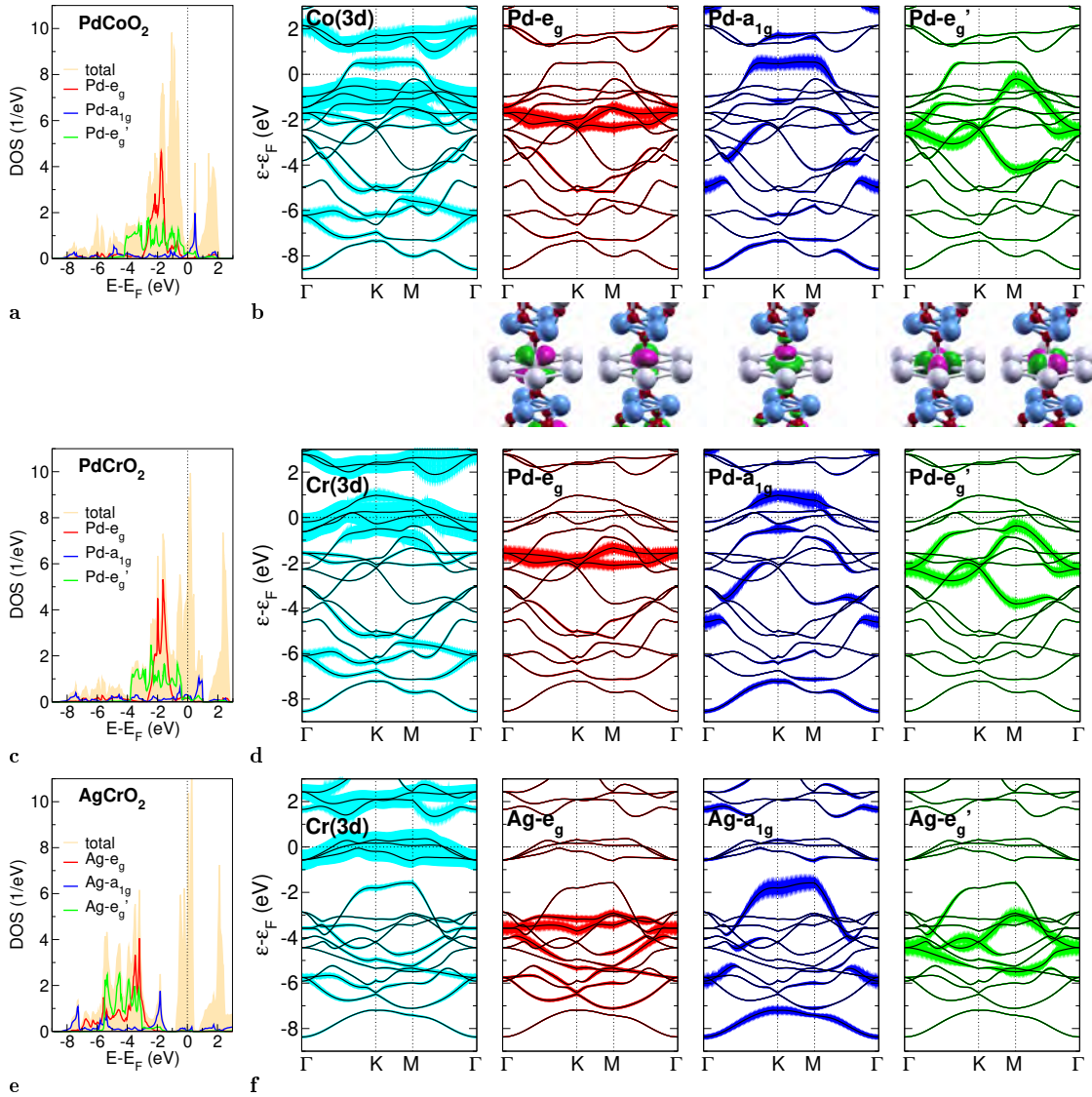
Fig. 10: *DFT electronic structure of PdCoO$_2$, PdCrO$_2$ and AgCrO$_2$. (a) Total and orbital-resolved $\mathcal{A}$-site$(4d)$ density of states. (b) Band structure along high symmetry lines in the $k_z = 0$ plane, with fatbands marking the $\mathcal{B}$-site$(3d)$ and the orbital-resolved $\mathcal{A}$-site$(4d)$ character. Additionally, the corresponding real-space Pd$(4d)$ projected local orbitals are provided for the case of PdCoO$_2$: Pd (grey), Cr (light blue) and O (red). (c, d) Same as (a, b) but for PdCrO$_2$. (e, f) Same as (a, b) but for AgCrO$_2$. From Ref. [57].*

Finally, the AgCrO$_2$ compound would be insulating in DFT if the Cr-t_{2g} states were not located again at the Fermi level (see Figs. 10e, f). The Ag$(4d)$ states are filled and would give rise to a band insulator. The missing correlation effects on Cr become most evident here. The prominent Ag-a_{1g} dominated band just below the Cr-t_{2g} bands in energy and with a nearly flat dispersion along K-M bears striking resemblance to the former low-energy cPd band in PdCoO$_2$. In fact as we will see in the following, this present band will just form the highest valence band in true AgCrO$_2$ once correlations are properly included. Furthermore for the same reason, the akin band in PdCrO$_2$ (yet there with stronger Pd-e'_g character) will be shifted to ε_{F}.

5.2 Impact of correlation effects

For the charge self-consistent DFT+DMFT calculations the correlated subspace is build up from the five effective $\mathcal{B}$-site Wannier-like $3d$ functions as obtained from the projected-local-orbital formalism [15, 16], using as projection functions the linear combinations of atomic $3d$ orbitals which diagonalize the $\mathcal{B}$-site $3d$ orbital-density matrix. A five-orbital Slater-Kanamori Hubbard Hamiltonian, i.e., including density-density, spin-flip and pair-hopping terms, is utilized in the correlated subspace, parametrized by a Hubbard U and a Hund exchange J_{H}. The $\mathcal{B}$ site will here be either of Co or Cr type and a value of $J_{\mathrm{H}} = 0.7\,\mathrm{eV}$ is proper for TM oxides of that kind. Concerning the Hubbard interaction, the value $U = 3\,\mathrm{eV}$ is assigned to the $3d$ states of Co and Cr in $PdCoO_2$ and $PdCrO_2$, respectively [73, 74]. For $Cr(3d)$ in $AgCrO_2$, the somewhat larger value of $U = 4\,\mathrm{eV}$ is used in order to comply with the weaker screening because of the (nearly) filled $Ag(4d)$ shell. Note that no further Hubbard interactions are assigned to the $\mathcal{A}$ site. The d orbitals on those sites are here of $4d$ kind, of formal d^9 filling and only weakly hybridizing with oxygen. Thus by any means, Coulomb interactions are expected much smaller than on the $\mathcal{B}$ site. Spin-orbit coupling is neglected in the crystal calculations. Though the $\mathcal{A}CrO_2$ delafossites order antiferromagnetically at low temperatures within the CrO_2 layers, the investigations remain at still higher T assuming paramagnetism for all studied cases. If not otherwise stated, the system temperature is set to $T = 290\,\mathrm{K}$. Further details on the calculational settings can be found in Ref. [57] and see also Refs. [64, 75].

Figure 11 exhibits the spectral DFT+DMFT summary for the three compounds. In the case of the Co compound, the changes compared to DFT appear minor, as already expected from the simplest picture of a closed Co-t_{2g} subshell. The dispersions, which now describe true quasi-particle features, are hardly modified at lower energy. Quite on the contrary, the QP dispersion for $PdCrO_2$ has changed dramatically (see Fig. 11b); the DFT-original Cr bands at ε_{F} have disappeared and instead, a single cPd dispersion as in $PdCoO_2$ crosses the Fermi level. This result brings theory eventually in line with experimental findings [68, 63, 69, 70]. Also for $AgCrO_2$, the DFT+DMFT approach settles the comparison with experiment, namely by identifying the insulating nature with a compatible gap of $\sim 1.8\,\mathrm{eV}$. While the latter delafossite shows of course no Fermi surface, the fermiology of $PdCoO_2$ and $PdCrO_2$ in Figs. 11d,e becomes rather similar with interactions. A single-sheet interacting Fermi surface, comprising a single electron, is centered around Γ and has a hexagonal shape with some warping. Note that this warping is somewhat stronger in the case of the Co compound.

Two functions are provided to discuss the $\mathbf{k}$-integrated spectra (see Fig. 11h-j). First, the site- and orbital-projected spectral function $A_{\mathrm{proj}}(\omega)$, defined by projecting the Bloch-resolved spectral function $A_\nu(\mathbf{k}, \omega)$ with Bloch index ν onto a chosen site-orbital and summing over $\nu, \mathbf{k}$. Note that this function is comparable but strictly not identical to the local spectral function A_{loc}, which is obtained from analytical continuation of the local Green function. Second, it proves instructive to also plot directly $A_\nu(\omega)$, i.e., the $\mathbf{k}$-integrated Bloch-resolved spectrum. This allows us to trace the behavior of the former DFT bands upon interaction and displays the QP formation originating in Bloch space.
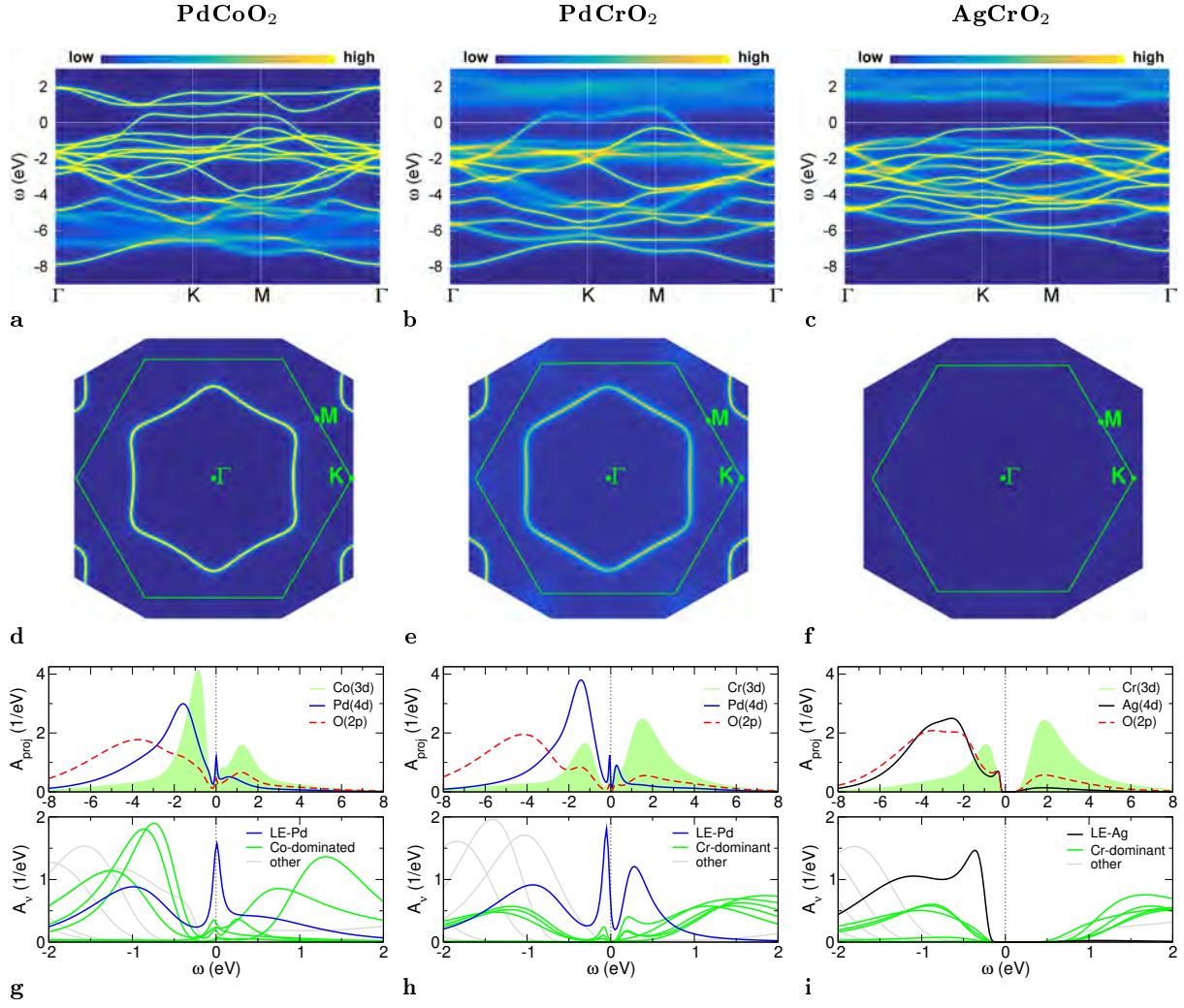
Fig. 11: *Spectral properties of PdCoO$_2$, PdCrO$_2$ and AgCrO$_2$ from paramagnetic DFT+DMFT. (a-c) **k**-resolved spectral function $A(\mathbf{k}, \omega)$ along high symmetry lines in the $k_z = 0$ plane. (d-f) Interacting Fermi surface in the $k_z = 0$ plane. (g-i) Site- and orbital-projected spectral function $A_{\mathrm{proj}}(\omega)$ (top) and Bloch-resolved spectral function $A_\nu(\omega)$, see text (bottom), respectively. From Ref. [57].*

The projected spectrum of PdCoO$_2$ exhibits the near subshell filling of Co($3d$) and the Pd dominance of the low-energy QP peak at the Fermi level. In PdCrO$_2$, the Cr-t_{2g} states are in a Mott state and therefore their spectral weight is shifted to upper and lower Hubbard bands. The Cr-e_g states are mostly empty, but show also strong incoherence effects in Fig. 11b. Mott criticality in the CrO$_2$ layers has been originally suggested by several experiments from strong hints for localized Cr^{3+} $S = 3/2$ spins [76, 63, 70]. The QP peak at low energy is of dominant Pd($4d$) character, therefore confirming the previously announced mechanism of a correlation-induced shift of a DFT-original deeper lying Pd-dominated band towards ε_{F}. The projected AgCrO$_2$ spectrum shows again the Mott-insulating Cr($3d$) part along with the band-insulating Ag($4d$) part. The plots of $A_\nu(\omega)$ render obvious that for PdCoO$_2$ the low-energy QP is for the most

part constituted from a single Pd-dominated Bloch dispersion, which we call LE-Pd. The same holds for the PdCrO$_2$ case. Yet importantly, both QP peaks display the hybridizing contribution of Co/Cr-dominated functions, and the LE-Pd function moreover exhibits significant energy dependence. Both features point to the relevance of the subtle impact of electronic correlation onto the low-energy regime. Or in other words, the 'single-band' dispersion crossing ε_F, though not dominated by the strongly-interacting $\mathcal{B}$-site $3d$ orbitals, still carries subtle effects of correlations which most certainly rule (parts of) the challenging delafossite physics. But be aware of our difference in nomenclature; 'cPd' denotes the complete single low-energy dispersion, while 'LE-Pd' marks the most dominant A_ν contribution to it.

The impact of electronic correlations is especially crucial and intriguing for PdCrO$_2$. On a more formal level, interactions lead to a metal-to-metal transition between a system with Cr($3d$)-dominated threefold dispersion at weak coupling and a system with Pd($4d$)-dominated single dispersion at strong coupling. The question arises how this apparent quantum phase transition takes place with increasing interaction strength U. Figure 12a displays the spectral function and fatbands for the DFT limit ($U = 0$) and for $U = 1.5$ eV, i.e., half the assumed correct interaction strength in PdCrO$_2$. The comparison renders the mechanism for the transition clear: The three bands at the Fermi level are filled with two electrons, and hence four electrons populate the altogether four bands when counting down in energy from ε_F. These four bands are of mixed Cr($3d$), Pd($4d$) character, with dominance from the $3d$ sector. Due to the given band entanglement, strong correlations transform three of them into Hubbard bands, and leave a resulting one with half filling at the Fermi level. Interestingly, for the intermediate coupling (right panel of Fig. 12a), the system adopts a 'strange' situation. The Cr-t_{2g} dispersions are very incoherent and not yet Mott localized, and the cPd dispersion is not yet fully established coherently. Note that especially the latter dispersion, which appears weakly-interacting at strong and weak coupling, is intriguingly affected by correlations close to the given metal-to-metal transition. This underlines the intricate inter-layer physics that is at work in PdCrO$_2$ with its 'hidden-Mott' state.

From a model perspective of correlated electrons, Kondo-lattice type of Hamiltonians describing strongly-interacting sites within a Fermi sea [77, 78] have been discussed as a starting perspective for PdCrO$_2$ [64]. Such a framework has then indeed been put into practice in order to account for the coupling of the Cr spins to the Pd layer in the magnetically-ordered state [65]. However, as already mentioned in Ref. [64], a standard Kondo-lattice model of spins coupled to free electrons appears too simplistic to cover the full complexity of the above described hidden-Mott physics [79]. Modelling the electronic correlations that originate from the CrO$_2$ layer and spanning over to the Pd layer in a comprehensive way has most definitely to account for the outlined metal-to-metal transition.

Because of the $4d^{10}$ state of silver in AgCrO$_2$, an intricate band entanglement as in PdCrO$_2$ is missing. In the DFT limit, the three Cr-t_{2g} bands at the Fermi level are already half filled with three electrons. Thus the internal Mott transition in the CrO$_2$ layers does not lead to a metal-to-metal transition, but to a more ordinary metal-to-insulator transition with increasing U. But there is a twist; the valence-band maximum of insulating AgCrO$_2$ is dominated by silver (and
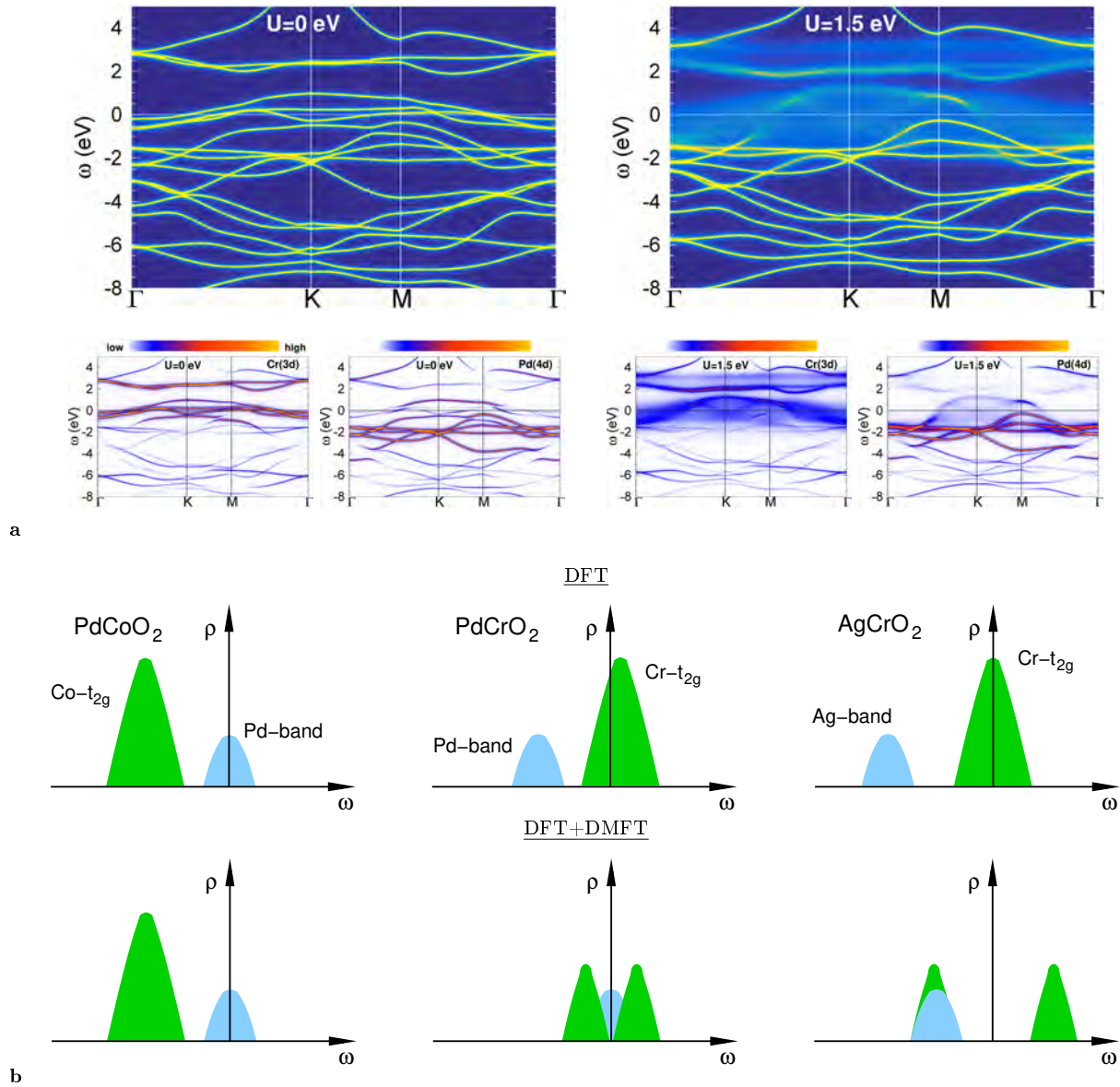
Fig. 12: *Correlation features in delafossites. (a) Spectral properties of PdCrO$_2$ for different interaction strengths. Left panel: $U = 0\,eV$, i.e., DFT bands. Right panel: $U = 1.5\,eV$. Top: spectral function, bottom: fatbands for Cr(3d) (left) and Pd(4d) (right) (from [75]). (b) Sketch of the basic differences in the **k**-integrated spectral function $\rho(\omega)$ for the most-relevant four bands close to the Fermi level among the studied delafossites. Top: DFT, bottom: DFT+DMFT. Left: PdCoO$_2$: Co-t$_{2g}$ bands occupied, uppermost Pd(4d)-band half filled; middle: hidden-Mott PdCrO$_2$: Cr-t$_{2g}$ bands 1/3 filled, uppermost Pd(4d)-band occupied; right: band-Mott insulating AgCrO$_2$: Cr-t$_{2g}$ bands half filled, uppermost Ag(4d)-band occupied. From Ref. [57].*

oxygen) character, highlighting the band-insulating aspect of the system. The compound is therefore best coined as band-Mott insulator.

To emphasize the key differences of the given delafossites from a minimal perspective, Fig. 12b summarizes the main features from the noted four-band perspective of $\mathcal{B}$-site derived t_{2g} bands and $\mathcal{A}$-site derived uppermost $4d$ band part.
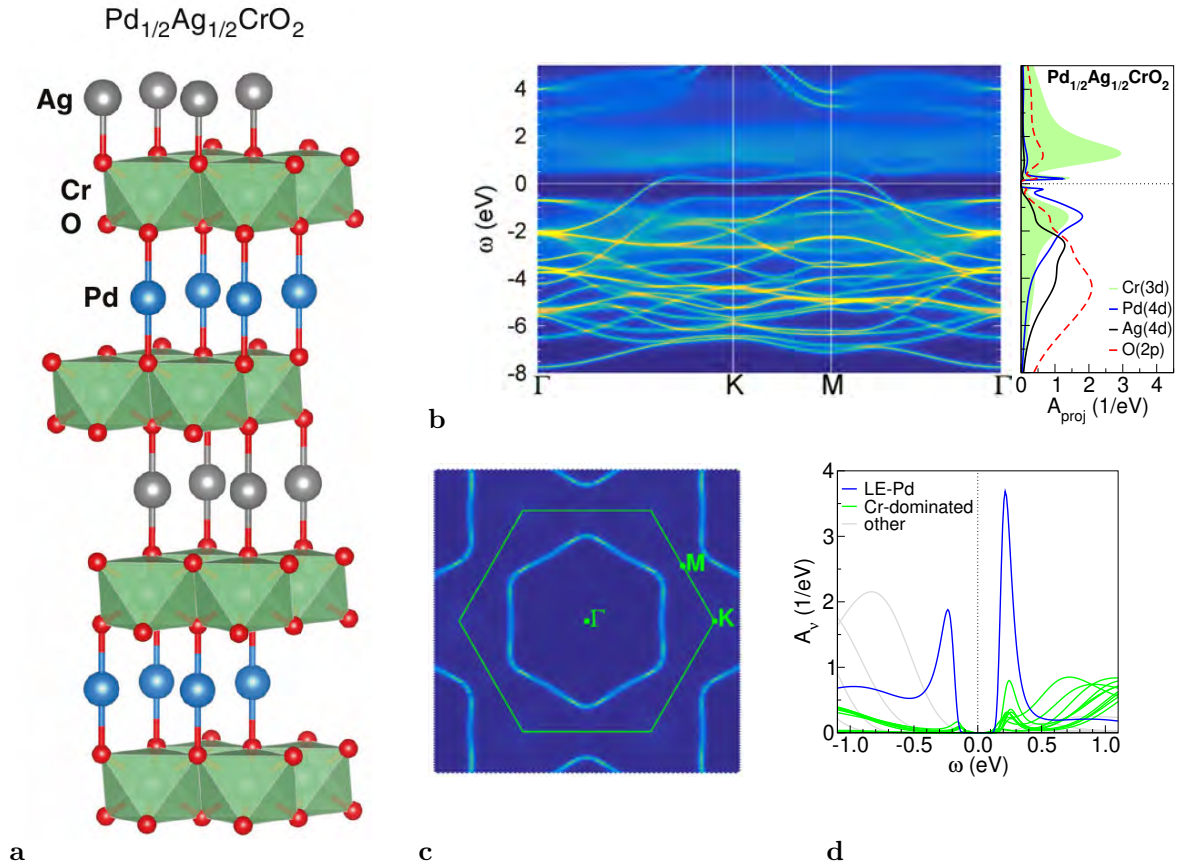
Fig. 13: *Paramagnetic DFT+DMFT spectral data for the out-of-plane heterostructure.* $Pd_{1/2}Ag_{1/2}CrO_2$. *(a) Crystal structure, with Pd: blue, Ag: grey, Cr: green and O: red. (b) Spectral function $A(\mathbf{k}, \omega)$ along high-symmetry lines in the $k_z = 0$ plane of reciprocal space (left) and $\mathbf{k}$-integrated site- and orbital-projected spectral function (right). (c) Fermi surface for $k_z = 0$ within the first Brillouin zone (green hexagon). (d) $\mathbf{k}$-integrated Bloch contribution $A_\nu(\omega)$ with characterization of dominance. After Ref. [75].*

5.3 Theoretical Mott design

As noted earlier, delafossites may be viewed as natural heterostructures with different electronic characteristics in the $\mathcal{A}$- and $\mathcal{B}O_2$-layers. It may be therefore obvious that a merging of delafossite physics and the explicit field of oxide heterostructures could turn out as a fruitful combination. In fact, heterostructures from combining $PdCrO_2$ and $AgCrO_2$ may be of particular interest. Both compounds have similar lattice parameters, resulting in a minor mismatch, and differ only by one electron in the $\mathcal{A}$-site valence. However their electronic phenomenology, i.e., hidden-Mott metal vs. band-Mott insulator, is quite different. Heterostructuring both delafossites provides therefore a specific doping scenario: by keeping the local environment rather undisturbed, filling modifications in the Cr-t_{2g} manifold may be triggered.

Alternate stackings of Pd, CrO_2 and Ag layers, i.e., straightforward out-of-plane heterostructures, are a natural realization of such a scenario. Let us discuss a specific $PdCrO_2/AgCrO_2$ stacking along the c-axis, namely $Pd_{1/2}Ag_{1/2}CrO_2$ (see Fig. 13a), with the Hubbard U (identical

on every Cr site) being also correspondingly interpolated from the limiting delafossite cases (see Ref. [75] for further details). From the $PdCrO_2$ perspective, the additional blocking layers of Ag kind as well as the stronger Mott-insulating character induced therefrom into the CrO_2 layers should increase correlations within the Pd layers, too. But this will again happen in a more subtle way than in standard correlated systems, where an associated Coulomb repulsion for such a layer is increased when looking for stronger correlation effects. Remember that there is no Hubbard U on Pd and all correlation increase has to take place in a "nonlocal" way from the surrounding layers. Thus, the present heterostructures pose a quite original correlation problem at low energy; a half-filled Pd layer without intra-layer interaction, subject to rising 'Coulomb pressure and confinement' imposed from the neighboring layers. How does the single electron of dominant $Pd(4d)$ character cope with that situation?

Figure 13 displays the DFT+DMFT spectral properties at room temperature for the given meta-heterostructure. A detailed discussion, also concerning stability issues and with extension to lower-temperature properties, can be found in Ref. [75]. The main result, may be extracted from the low-energy comparison of the $\mathbf{k}$-resolved and the $\mathbf{k}$-integrated data: while there are still QP-like dispersions visible in $A(\mathbf{k}, \omega)$ at the Fermi level, the integrated spectra shows vanishing spectral weight at ε_F. We coin this puzzling electronic state as correlation-induced semimetal (CIS), which is obviously a result of the intriguing correlation scenario described above. Upon rising obstruction of transport, the key $Pd(4d)$ electron can neither localize in real space (as in a Mott insulator) nor rest in a filled band (as in a band insulator). Hence it reduces the low-energy spectral weight as much as possible for an intact half-filled band, resulting in the CIS state. Note that this finding is not an artifact of the analytical continuation from Matsubara space to real frequencies, as the result is confirmed from both, maximum-entropy as well as Padé methods [75] and therefore a robust feature. In some sense it amounts to a very strong reduction of the usual QP coherence scale of strongly correlated electrons, yet by still keeping the 'coherence' of the original dispersion. To our knowledge, such a rather exotic electronic state has not yet been reported in correlated matter and it awaits experimental verification.

Finally, let us push the limits of conceivable delafossite engineering even somewhat further, by interpreting the metallic implication of Pd in $PdCrO_2$ and the band-insulating implication of Ag in $AgCrO_2$ theoretically footloose. Instead of engineering $PdCrO_2$ 'out of plane' from replacing Pd layers by Ag layers, one may imagine an 'in-plane' alternation from replacing Pd sites by Ag sites in the periodically-repeated $\mathcal{A}$ layer. As a result, a novel natural-heterostructure delafossite emerges, but now with a decorated $\mathcal{A}$ layer. The viewpoint behind arises from picturing the $\mathcal{A}$ layer in hidden-Mott delafossite as a canonical single-band triangular lattice at half filling, embedded in a Mott-insulating background. By manipulating the features of this triangular lattice, a platform for studying correlation effects in such a Mott background may be generated. The simplest manipulations in this regard are given by the straightforward transformations of the original triangular lattice via the K- and M-point ordering instabilities, associated with the honeycomb (K) and the kagomé (M) lattice (see Fig. 14a). Realizing those lattices within a Mott background is exciting because they host Dirac-semimetallic and, in the case of the kagomé lattice, additionally flat-band dispersions. The study of these dispersion features under
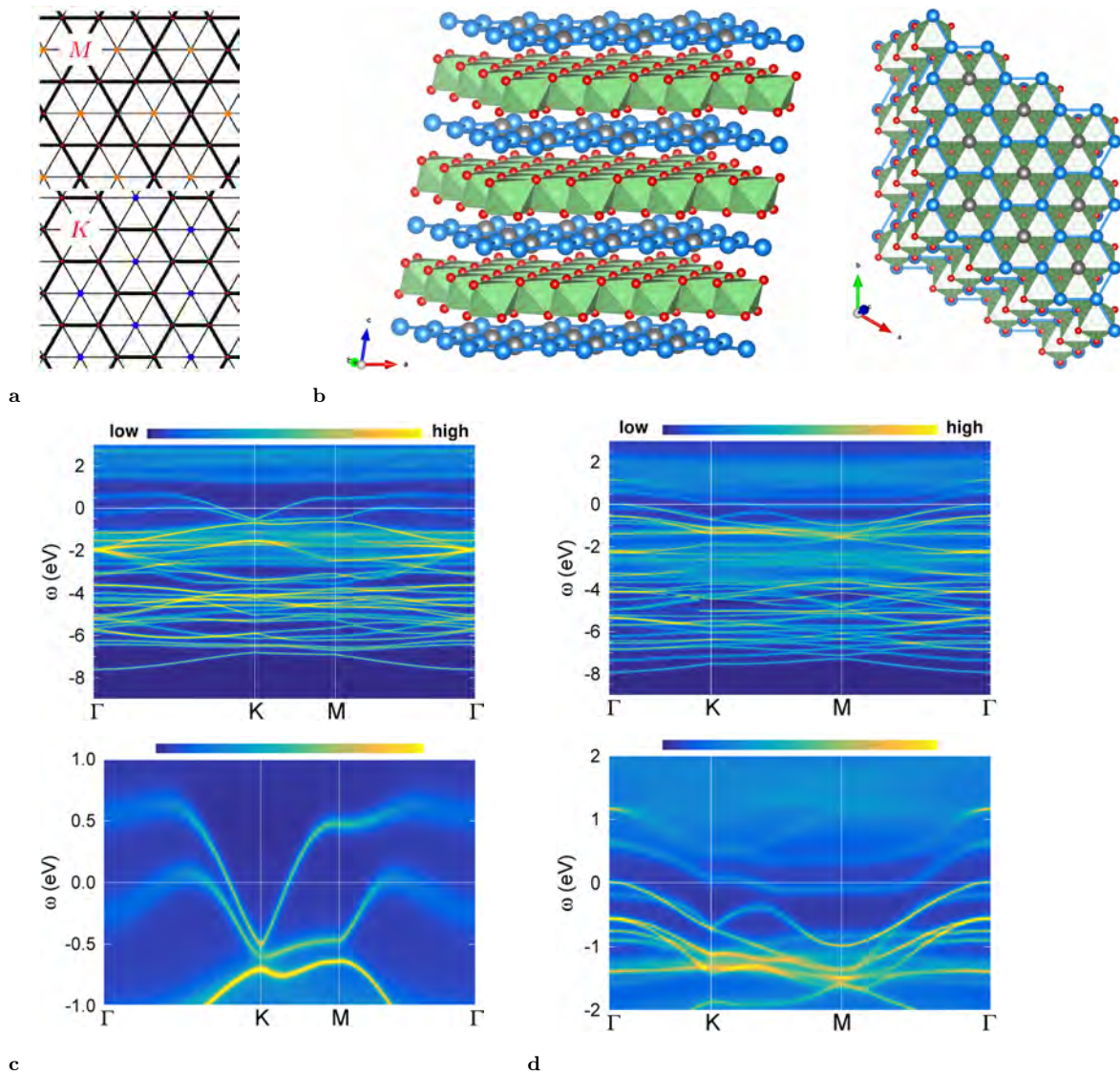
Fig. 14: *Effective-honeycomb and -kagomé (Pd,Ag)CrO$_2$ delafossite. (a) In-plane design of the $\mathcal{A}$ layer via the natural triangular-lattice ordering instabilities of K-point (honeycomb) and M-point (kagomé) kind (from [80]). (b) Designed crystal structure from understanding Pd(Ag) positions as active(blocking) sites; Pd: blue, Ag: grey, O: red; Cr: green. Left: 3D view and right: view onto the effective honeycomb lattice of Pd sites. (c, d) Interacting spectral information from DFT+DMFT at $T = 193$ K. (c) Spectral function in (top) larger and (bottom) smaller energy window for effective-honeycomb structure. (d) same as (c) but for effective-kagomé structure.*

the possible influence of strong correlations is a recent emerging research field in condensed matter, see e.g. Refs. [81–83].

To facilitate this reductions of the triangular lattice, the introduction of periodic blocking sites which ideally disconnect hopping processes, can be a promising route. From the nominal Ag($4d$) filled-shell in the CrO$_2$-based delafossites, we assume in the present context that Ag sites within the Pd layer may serve as such blocking sites. For sure, finite covalency will only realize a partial blocking, however, this may still be sufficient to mimic basic honeycomb- or

kagomé-lattice features. To realize a honeycomb(kagomé) lattice in that spirit within the $\mathcal{A}$ layer, one out of three(four) in-plane Pd sites has to be replaced by Ag. Note that though preparing such orderings in the lab will be surely demanding, a layer-by-layer growth might still be feasible from tailoring the layer stoichiometry. If the given Pd-Ag in-plane orderings are thermodynamically stable (for given temperature, pressure, strain, etc.), nature will take its course in realizing the periodic effective honeycomb/kagomé pattern. For the honeycomb case, Fig. 14b depicts the designed delafossite structure. The DFT+DMFT calculations for both effective-lattice systems are again performed with corresponding linear interpolation of the chosen Hubbard U values for the bulk compounds. The honeycomb(kagomé) structure asks for a supercell of three(four) original formula units. Note that we utilized a somewhat lower system temperature of $T = 193$ K for both structural cases, since from general inspection of the spectral properties, the coherence scale for stable quasiparticles appears smaller for the given in-plane alternations compared to the out-of-plane heterostructures.

In Fig. 14c,d we show the resulting spectral functions. From graphene studies it is well known that the nearest-neighbor (NN) tight-binding electronic structure of the half-filled honeycomb lattice is semimetallic, with prominent Dirac dispersions (i.e. massless Dirac fermions) at the K point in reciprocal space [84]. The low-energy spectrum of the present effective-honeycomb lattice in the delafossite setting shows indeed some resemblance of this feature. First, the CrO_2 planes remain Mott-insulating upon the in-plane (Pd, Ag) structuring and there are two Pd-dominated dispersions close to ε_F (see Fig. 14a). A Dirac-like dispersion around K is indicated, yet shifted, with different filling and different overall dispersion compared to graphene. Still, some blocking behavior of Ag is realized, transforming the original $PdCrO_2$ low-energy dispersion in direction towards the canonical honeycomb dispersion. The NN tight-binding electronic structure of the kagomé lattice is known for its flat-band feature at one side of the band edge, as well as for the Dirac dispersion at 4/3 (2/3) filling, depending on the sign of the NN hopping (e.g. [81]). In the present case, the flat-band feature should appear at the upper band edge and thus the Dirac point at 2/3 filling. Figure 14d depicts the resulting spectral function of effective-kagomé $(Pd,Ag)CrO_2$, and from a brief look the canonical kagomé features are hard to decipher. The intriguing effect of correlations and only-partial Ag blocking render things hard to read. Yet after a closer look, and after also comparing with the non-interacting DFT states, the remains of the flat-band feature can be located around 1 eV above the Fermi level. Interestingly, the interactions in the delafossite structure seemingly transfer spectral weight from there towards ε_F. Close to Γ, a waterfall-like spectral signature may be observed. Hence a flat, but at $T = 193$ K rather incoherent, low-energy feature ranging from K to M and halfway to Γ emerges. The Dirac-dispersion feature at K from the canonical kagomé lattice can also be identified at about -0.6 eV.

In conclusion, expectedly neither the effective-honeycomb nor the effective-kagomé lattice realization in the modified $PdCrO_2$ structure enables canonical textbook dispersions at the Fermi level. But as a proof of principle, the in-plane engineering of delafossites may be a route to create nontrivial low-energy dispersions which are subject to the puzzling layer-entangled correlation delafossite physics.

6   Further systems

So far, the present review mainly focussed on early transition-metal titanate heterostructures, but theoretical work also dealt with other oxide designs. For instance, the late-transition-metal rare-earth (R) nickelate series $R\mathrm{NiO_3}$ provides important material building blocks, too [85]. Originally, there was the idea to realize cuprate-like physics within nickelates by proper heterostructuring [86, 87], however experimental success remained absent for a long time. It was only 2019 that Li *et al.* detected superconductivity in thin films of reduced $\mathrm{NdNiO_2}$ on an STO substrate [88]. If this superconducting state is cuprate-like is, however, still a matter of ongoing debate (see e.g. [89]).

Bulk perovskite-like vanadates split into correlated metals, e.g., $\mathrm{SrVO_3}$ and $\mathrm{CaVO_3}$, and Mott insulators, e.g., $\mathrm{LaVO_3}$ and $\mathrm{YVO_3}$. Heterostructures based on $\mathrm{SrVO_3}$ were studied in view of a possible loss of metallicity in a small-layer limit [90, 91]. Moreover, transition-metal oxides from the $4d$ and $5d$ series serve as further building blocks. For instance, the $4d^4$ physics of strontium and/or calcium ruthenates poses a longstanding problem, which can be tuned by heterostructuring [92].

7   Concluding remarks

We here provided a short overview on selected features of DFT+DMFT applications to oxide heterostructures, mainly guided by the author's own work. Note that especially the experimental side of this frontier field of condensed matter physics extends to various further phenomena, e.g., detailed magnetism engineering in interfaces, which can be found in other, more general reviews on the oxide-heterostructure topic.

From the DMFT perspective, one may state that present state-of-the-art DFT+DMFT is truly capable of addressing many challenges of oxide heterostructures. In other words, such 'large-scale' quantum materials science problems are not out of reach for first-principles many-body techniques. Of course, therefore one has to leave the 'safer ground' of model Hamiltonians or more straightforward bulk scenarios. Hence especially in such a regime, DFT+DMFT is not a 'black-box' machinery, but physical intuition and careful weighing of the calculational setting (i.e. choice of correlated subspace, etc.) goes hand in hand with demanding numerics. But this may not be seen as a contradicting endeavor, but quite on the contrary: heavy numerics guided by proper physical insight seems indispensable to tackle the multiorbital and multisite correlated electron problem of oxide heterostructures and related modern materials complexities.

References

[1] J.N. Eckstein and I. Bozovic, Annu. Rev. Mater. Sci. **25**, 679 (1995)

[2] A. Ohtomo and H.Y. Hwang, Nature **427**, 423 (2004)

[3] S. Stemmer and A.J. Millis, MRS Bulletin **38**, 1032 (2013)

[4] D. Lu, D.J. Baek, S.S. Hong, L.F. Kourkoutis, Y. Hikita, and H.Y. Hwang,
Nat. Mater. **15**, 1255 (2016)

[5] H.Y. Hwang, Y. Iwasa, M. Kawasaki, B. Keimer, N. Nagaosa, and Y. Tokura,
Nat. Mater. **11**, 103 (2012)

[6] P. Zubko, S. Gariglio, M. Gabay, P. Ghosez, and J.-M. Triscone,
Annu. Rev. Condens. Matter Phys. **2**, 141 (2011)

[7] J. Chakhalian, J.W. Freeland, A.J. Millis, C. Panagopoulos, and J.M. Rondinelli,
Rev. Mod. Phys. **86**, 1189 (2014)

[8] B. Keimer and J.E. Moore, Nat. Phys. **13**, 1045 (2017)

[9] W. Metzner and D. Vollhardt, Phys. Rev. Lett. **62**, 324 (1989)

[10] A. Georges and G. Kotliar, Phys. Rev. B **45**, 6479 (1992)

[11] M. Imada, A. Fujimori, and Y. Tokura, Rev. Mod. Phys. **70**, 1039 (1998)

[12] A. Georges, G. Kotliar, W. Krauth, and M.J. Rozenberg, Rev. Mod. Phys. **68**, 13 (1996)

[13] V.I. Anisimov, A.I. Poteryaev, M.A. Korotin, A.O. Anokhin, and G. Kotliar,
J. Phys.: Condens. Matter **9**, 7359 (1997)

[14] A.I. Lichtenstein and M. Katsnelson, Phys. Rev. B **57**, 6884 (1998)

[15] B. Amadon, F. Lechermann, A. Georges, F. Jollet, T.O. Wehling, and A.I. Lichtenstein,
Phys. Rev. B **77**, 205112 (2008)

[16] V.I. Anisimov, D.E. Kondakov, A.V. Kozhevnikov, I.A. Nekrasov, Z.V. Pchelkina,
J.W. Allen, S.-K. Mo, H.-D. Kim, P. Metcalf, S. Suga, A. Sekiyama, G. Keller,
I. Leonov, X. Ren, and D. Vollhardt, Phys. Rev. B **71**, 125119 (2005)

[17] S.Y. Savrasov, G. Kotliar, and E. Abrahams, Nature **410**, 793 (2001)

[18] J. Minár, L. Chioncel, A. Perlov, H. Ebert, M.I. Katsnelson, and A.I. Lichtenstein,
Phys. Rev. B **72**, 045125 (2005)

[19] L.V. Pourovskii, B. Amadon, S. Biermann, and A. Georges,
Phys. Rev. B **76**, 235101 (2007)

[20] D. Grieger, C. Piefke, O.E. Peil, and F. Lechermann, Phys. Rev. B **86**, 155121 (2012)

[21] F. Lechermann, A. Georges, A. Poteryaev, S. Biermann, M. Posternak, A. Yamasaki, and O.K. Andersen, Phys. Rev. B **74**, 125120 (2006)

[22] M. Potthoff and W. Nolting, Phys. Rev. B **59**, 2549 (1999)

[23] B. Meyer, C. Elsässer, F. Lechermann, and M. Fähnle: *FORTRAN 90 Program for Mixed-Basis-Pseudopotential Calculations for Crystals* (2012)

[24] P. Werner, A. Comanac, L. de' Medici, M. Troyer, and A.J. Millis, Phys. Rev. Lett. **97**, 076405 (2006)

[25] P. Seth, I. Krivenko, M. Ferrero, and O. Parcollet, Comput. Phys. Commun. **200**, 274 (2016)

[26] N. Nakagawa, H.Y. Hwang, and D.A. Muller, Nat. Mater. **5**, 204 (2006)

[27] Y.Z. Chen, N. Bovet, F. Trier, D.V. Christensen, F.M. Qu, N.H. Andersen, T. Kasama, W. Zhang, R. Giraud, J. Dufouleur, T.S. Jespersen, J.R. Sun, A. Smith, J. Nygård, L. Lu, B. Büchner, B.G. Shen, S. Linderoth, and N. Pryds, Nat. Commun. **4**, 1372 (2013)

[28] N. Reyren, S. Thiel, A.D. Caviglia, L.F. Kourkoutis, G. Hammerl, C. Richter, C.W. Schneider, T. Kopp, A.-S. Rüetschi, D. Jaccard, M. Gabay, D.A. Muller, J.-M. Triscone, and J. Mannhart, Science **317**, 1196 (2007)

[29] A. Brinkman, M. Huijben, M. van Zalk, J. Huijben, U. Zeitler, J.C. Maan, W.G. van der Wiel, G. Rijnders, D.H.A. Blank, and H. Hilgenkamp, Nat. Mater. **6**, 493 (2007)

[30] F. Lechermann, L. Boehnke, D. Grieger, and C. Piefke, Phys. Rev. B **90**, 085125 (2014)

[31] M. Salluzzo, S. Gariglio, D. Stornaiuolo, V. Sessi, S. Rusponi, C. Piamonteze, G.M. DeLuca, M. Minola, D. Marré, A. Gadaleta, H. Brune, F. Nolting, N.B. Brookes, and G. Ghiringhelli, Phys. Rev. Lett. **111**, 087204 (2013)

[32] N. Pavlenko, T. Kopp, E.Y. Tsymbal, J. Mannhart, and G.A. Sawatzky, Phys. Rev. B **86**, 064431 (2012)

[33] G. Berner, M. Sing, H. Fujiwara, A. Yasui, Y. Saitoh, A. Yamasaki, Y. Nishitani, A. Sekiyama, N. Pavlenko, T. Kopp, C. Richter, J. Mannhart, S. Suga, and R. Claessen, Phys. Rev. Lett. **110**, 247601 (2013)

[34] A. Chikina, F. Lechermann, M.-A. Husanu, M. Caputo, C. Cancellieri, X. Wang, T. Schmitt, M. Radovic, and V.N. Strocov, ACS Nano **12**, 7927 (2018)

[35] M. Behrmann and F. Lechermann, Phys. Rev. B **92**, 125148 (2015)

[36] F. Lechermann, A. Georges, G. Kotliar, and O. Parcollet, Phys. Rev. B **76**, 155102 (2007)

[37] T. Li, P. Wölfle, and P.J. Hirschfeld, Phys. Rev. B **40**, 6817 (1989)

[38] F. Lechermann, H.O. Jeschke, A.J. Kim, S. Backes, and R. Valentí,
Phys. Rev. B **93**, 121103(R) (2016)

[39] A.F. Santander-Syro, O. Copie, T. Kondo, F. Fortuna, S. Pailhè, R. Weht, X.G. Qiu,
F. Bertran, A. Nicolaou, A. Taleb-Ibrahimi, P.L. Fèvre, G. Herranz, M. Bibes, N. Reyren,
Y. Apertet, P. Lecoeur, A. Barthélémy, and M.J. Rozenberg, Nature **469**, 189 (2011)

[40] W. Meevasana, P.D.C. King, R.H. He, S.-K. Mo, M. Hashimoto, A. Tamai,
P. Songsiriritthigul, F. Baumberger, and Z.-X. Shen, Nat. Mat. **10**, 114 (2011)

[41] S. McKeown Walker, A. de la Torre, F.Y. Bruno, A. Tamai, T.K. Kim, M. Hoesch, M. Shi,
M.S. Bahramy, P.C. King, and F. Baumberger, Phys. Rev. Lett. **113**, 177601 (2014)

[42] H. Tanaka, T. Matsumoto, T. Kawai, and S. Kawai, Jpn. J. Appl. Phys. **32**, 1405 (1993)

[43] F. Lechermann, L. Boehnke, and D. Grieger, Phys. Rev. B **87**, 241101(R) (2013)

[44] A. Ohtomo, D.A. Muller, J.L. Grazul, and H.Y. Hwang, Nature **419**, 378 (2002)

[45] S. Okamoto and A.J. Millis, Nature **428**, 630 (2004)

[46] H. Ishida and A. Liebsch, Phys. Rev. B **77**, 115350 (2008)

[47] A. Rüegg, S. Pilgram, and M. Sigrist, Phys. Rev. B **75**, 195117 (2007)

[48] K. Dymkowski and C. Ederer, Phys. Rev. B **89**, 161109(R) (2014)

[49] G. Sclauzero and C. Ederer, Phys. Rev. B **92**, 235112 (2015)

[50] F. Lechermann, Sci. Rep **7**, 1565 (2017)

[51] P. Moetakef, C.A. Jackson, J. Hwang, L. Balents, S.J. Allen, and S. Stemmer,
Phys. Rev. B **86**, 201102(R) (2012)

[52] C.A. Jackson, J.Y. Zhang, C.R. Freeze, and S. Stemmer, Nat. Commun. **5**, 4258 (2014)

[53] E. Mikheev, C.R. Freeze, B.J. Isaac, T.A. Cain, and S. Stemmer,
Phys. Rev. B **91**, 165125 (2015)

[54] F. Lechermann and M. Obermeyer, New J. Phys. **17**, 043026 (2015)

[55] P.B. Marshall, E. Mikheev, S. Raghavan, and S. Stemmer,
Phys. Rev. Lett. **117**, 046402 (2016)

[56] F. Lechermann, John von Neumann Institute for Computing (NIC) NIC Series **49** (2018)

[57] F. Lechermann, npj Comput. Mater. **7**, 120 (2021)

[58] R.D. Shannon, D.B. Rogers, and C.T. Prewitt, Inorg. Chem. **10**, 713 (1971)

[59] C.T. Prewitt, R.D. Shannon, and D.B. Rogers, Inorg. Chem. **10**, 719 (1971)

[60] D.B. Rogers, R.D. Shannon, and C.T. Prewitt, Inorg. Chem. **10**, 723 (1971)

[61] R. Daou, R. Frésard, V. Eyert, S. Hébert, and A. Maignan,
Sci. Technol. Adv. Mater. **18**, 919 (2017)

[62] A.P. Mackenzie, Rep. Prog. Phys. **80**, 032501 (2017)

[63] H.-J. Noh, J. Jeong, B. Chang, D. Jeong, H.S. Moon, E.-J. Cho, J.M. Ok, J.S. Kim,
K. Kim, B.I. Min, H.-K. Lee, J.-Y. Kim, B.-G. Park, H.-D. Kim, and S. Lee,
Sci. Rep. **4**, 3680 (2014)

[64] F. Lechermann, Phys. Rev. Mater. **2**, 085004 (2018)

[65] V. Sunko, F. Mazzola, S. Kitamura, S. Khim, P. Kushwaha, O.J. Clark, M. Watson,
I. Markovic, D. Biswas, L. Pourovskii, T.K. Kim, T.L. Lee, P.K. Thakur, H. Rosner,
A.G.R. Moessner, T. Oka, A.P. Mackenzie, and P.D.C. King, Sci. Adv. **6**, eaaz0611 (2020)

[66] H.-J. Noh, J. Jeong, J. Jeong, E.-J. Cho, S.B. Kim, K. Kim, B.I. Min, and H.-D. Kim,
Phys. Rev. Lett. **102**, 256404 (2009)

[67] C.W. Hicks, A.S. Gibbs, A.P. Mackenzie, H. Takatsu, Y. Maeno, and E.A. Yelland,
Phys. Rev. Lett. **109**, 116401 (2012)

[68] J.A. Sobota, K. Kim, H. Takatsu, M. Hashimoto, S.-K. Mo, Z. Hussain, T. Oguchi,
T. Shishidou, Y. Maeno, B.I. Min, and Z.-X. Shen, Phys. Rev. B **88**, 125109 (2013)

[69] J.M. Ok, Y.J. Jo, K. Kim, T. Shishidou, E.S. Choi, H.-J. Noh, T. Oguchi, B.I. Min,
and J.S. Kim, Phys. Rev. Lett. **111**, 176405 (2013)

[70] C.W. Hicks, A.S. Gibbs, L. Zhao, P. Kushwaha, H. Borrmann, A.P. Mackenzie, H. Takatsu,
S. Yonezawa, Y. Maeno, and E.A. Yelland, Phys. Rev. B **92**, 014425 (2015)

[71] K.P. Ong and D.J. Singh, Phys. Rev. B **85**, 134403 (2012)

[72] D. Billington, D. Ernsting, T.E. Millichamp, C. Lester, S.B. Dugdale, D. Kersh,
J.A. Duffy, S.R. Giblin, J.W. Taylor, P. Manuel, D.D. Khalyavin, and H. Takatsu,
Sci. Rep. **5**, 12428 (2015)

[73] M.A. Korotin, V.I. Anisimov, D.I. Khomskii, and G.A. Sawatzky,
Phys. Rev. Lett. **80**, 4305 (1998)

[74] F. Lechermann, Phys. Rev. Lett. **102**, 046403 (2009)

[75] F. Lechermann and R. Richter, Phys. Rev. Res. **2**, 013352 (2020)

[76] H. Takatsu, H. Yoshizawa, S. Yonezawa, and Y. Maeno, Phys. Rev. B **79**, 104424 (2009)

[77] N. Mott, Phil. Mag. **30**, 403 (1974)

[78] S. Doniach, Physica B **91**, 231 (1977)

[79] E.V. Komleva, V.Y. Irkhin, I.V. Solovyev, M.I. Katsnelson, and S.V. Streltsov,
Phys. Rev. B **102**, 174438 (2020)

[80] L. Boehnke and F. Lechermann, Phys. Rev. B **85**, 115128 (2012)

[81] I.I. Mazin, H.O. Jeschke, F. Lechermann, H. Lee, M. Fink, R. Thomale, and R. Valentí,
Nat. Commun. **5**, 4261 (2014)

[82] L. Ye, M. Kang, J. Liu, F. von Cube, C.R. Wicker, T. Suzuki, C. Jozwiak, A. Bostwick,
E. Rotenberg, D.C. Bell, L. Fu, R. Comin, and J.G. Checkelsky, Nature **555**, 638 (2018)

[83] N.J. Ghimire and I.I. Mazin, Nat. Mater. **19**, 137 (2020)

[84] P.R. Wallace, Phys. Rev. **71**, 622 (1947)

[85] J. Hwang, J. Son, J.Y. Zhang, A. Janotti, C.G. Van de Walle, and S. Stemmer,
Phys. Rev. B **87**, 060101(R) (2013)

[86] P. Hansmann, X. Yang, A. Toschi, G. Khaliullin, O.K. Andersen, and K. Held,
Phys. Rev. Lett. **103**, 016401 (2009)

[87] M.J. Han, X. Wang, C.A. Marianetti, and A.J. Millis, Phys. Rev. Lett. **107**, 206804 (2011)

[88] D. Li, K. Lee, B.Y. Wang, M. Osada, S. Crossley, H.R. Lee, Y. Cui, Y. Hikita,
and H.Y. Hwang, Nature **572**, 624 (2019)

[89] M. Norman, Physics **13**, 85 (2020)

[90] S. Okamoto, Phys. Rev. B **84**, 201305(R) (2011)

[91] Z. Zhong, M. Wallerberger, J.M. Tomczak, C. Taranto, N. Parragh, A. Toschi,
G. Sangiovanni, and K. Held, Phys. Rev. Lett. **114**, 246401 (2015)

[92] L. Si, O. Janson, G. Li, Z. Zhong, Z. Liao, G. Koster, and K. Held,
Phys. Rev. Lett. **119**, 026402 (2017)